Chinese Chemical Letters 31 (2020) 579–582

Contents lists available at ScienceDirect

Chinese Chemical Letters

journal homepage: www.elsevier.com/locate/cclet

Communication

Water-in-salt electrolyte ion-matched N/O codoped porous carbons for high-performance supercapacitors

Jingjing Yan[a], Dazhang Zhu[a], Yaokang Lv[b], Wei Xiong[c], Mingxian Liu[a,d,*], Lihua Gan[a,*]

[a] Shanghai Key Lab of Chemical Assessment and Sustainability, School of Chemical Science and Engineering, Tongji University, Shanghai 200092, China
[b] College of Chemical Engineering, Zhejiang University of Technology, Hangzhou 310014, China
[c] Key Laboratory for Green Chemical Process of Ministry of Education, School of Chemistry and Environmental Engineering, Wuhan Institute of Technology, Wuhan 430073, China
[d] College of Chemistry and Molecular Engineering, Zhengzhou University, Zhengzhou 450001, China

ARTICLE INFO

Article history:
Received 11 April 2019
Received in revised form 7 May 2019
Accepted 20 May 2019
Available online 20 May 2019

Keywords:
N/O Codoped Porous carbon
Water-in-salt electrolyte
Pore/ion size matching
Symmetrical supercapacitor
High energy density

ABSTRACT

Pore size and distribution in carbon-based materials are regarded to be a key factor to affect the electrochemical capacitive performances of the resultant electrodes. In this study, nitrogen and oxygen codoped porous carbons (NOPCs) are fabricated based on a simple Schiff-base reaction between *m*-phenylenediamine and terephthalaldehyde. The NOPCs have tunable morphologies, high surface areas, abundant heteroatom doping. More importantly, the carbons show a dominant micropores of 0.5–0.8 nm, comparable to the ionic sizes of LiTFSI (Li^+ 0.069 nm; TFSI– 0.79 nm) water-in-salt electrolyte with a high potential window of 2.2 V. Consequently, the fabricated symmetric supercapacitor gives a high energy output of 30.5 Wh/kg at 1 kW/kg, and high stability after successive 10,000 cycles with ~96.8% retention. This study provides promising potential to develop high-energy supercapacitors.

Supercapacitors are promising candidates for energy storage devices due to their merits of exceptionally fast charge/discharge rate, excellent cycle life and high power density [1–6]. Carbon materials, with many advantageous properties such as large surface area, various morphologies, good endurance to both basic and alkaline solution, are widely applied for supercapacitor electrodes [7–11]. Among various carbons, carbon spheres show the advantages of regular morphology, good liquidity, tunable porosity and particle size, and have been proven as superior electrode materials [12,13]. Recently experimental and simulated studies have demonstrated that pore size and distribution have a profound effect on the buffering and transfer of electrolyte ions [14–16]. A representative example stands out where the electrochemical capacitance exhibits an unusual promotion as the pore size well matches the dimensionality of the electrolyte ions [17–20]. Besides, the electrode performances are not only related to the morphologies and pore structures of carbons, but also to the surface functionalization. Heteroatom (*e.g.*, N, P and O) doped carbons can achieve high capacitive performance owing to improved wettability, electrical conductivity and additional Faraday capacitance [21,22].

Except for electrode materials, electrolyte is another key factor to affect the energy/power outputs of the fabricated devices. Because of high ionic conductivity and price advantage, aqueous H_2SO_4, KOH, and Na_2SO_4 are the most frequently used electrolytes. However, they face a demerit of narrow potential range of water, which cause much difficulty to fabricate high-energy-density supercapacitors [23–25]. Recently, several electrolytes with an enlarged operating voltage (~2.0 V) are proposed, such as Li_2SO_4 [17] and $NaNO_3$ [26]. Using gold current collectors, Fic and *co*-workers reported a wide voltage window of 1 mol/L Li_2SO_4 (0–2.2 V) with a slight polarization at high voltage originating from water oxidation/reduction [27]. More recently, highly concentrated "water-in-salt" (WIS) is emerged as a kind of safe and high-voltage electrolytes. For example, Dou *et al.* reported that a high-voltage (2.2 V) of 21 mol/kg (mol-salt in kg-solvent) lithium bis(trifluoromethane sulfonyl)imide (LiTFSI) solution with excellent capacitive properties [28]. In the solvation shell of WIS electrolytes, the quantity of water molecules is much lower compared with lower salt concentration, along with very different interphasial region structure [29–31]. Such a unique feature is attributed to the superior electrochemical stability of the low-concentration H_2O molecules which have a strong coordination with Li^+ ions and nearly fully take part in Li^+ solvation sheaths, thereby inhibiting the water activity and resulting in an enlarged potential range.

* Corresponding Authors.
E-mail addresses: liumx@tongji.edu.cn (M. Liu), ganlh@tongji.edu.cn (L. Gan).

https://doi.org/10.1016/j.cclet.2019.05.035

In this work, we report *p*-toluenesulfonic acid-assisted amine-aldehyde Schiff-base towards N/O codoped porous carbons (NOPCs) for high-performance supercapacitors. The synthetic strategy is very simple, involving room-temperature polymerization and common one-step carbonization/activation, without any template, high-temperature and/or long-time reaction. A typical NOPCs comprise interconnected carbon spheres, which offer a conductive network to accelerate charge diffusion and improve electrochemical stability. Besides, NOPCs with high surface areas exhibit a dominant micropores of 0.5–0.8 nm, comparable to the ionic sizes of LiTFSI (Li^+/TFSI– 0.069/0.79 nm [32]) water-in-salt electrolyte with a high potential window of 2.2 V. As a result, the assembled symmetric supercapacitor yields a high energy density of 30.5 Wh/kg at 1 kW/kg, companied with a high stability after 10,000 cycles.

Scanning electron microscopy (SEM) images shown in Fig. 1 indicate the morphologies of the NOPCs are strongly dependent on the ratios of *m*-phenylenediamine (PLD) to terephthalaldehyde (TPA). $NOPC_{0.5}$ (sample denotation was shown in Supporting information) consists of uniform carbon sphere with diameter *ca.* 500 nm (Fig. 1a). With the increase of the ratio of PLD/TPA, the spheres in the sample $NOPC_1$ become interconnected (Fig. 1b), or with the presence of obvious sheet-like morphology in $NOPC_2$ (Fig. 1c). The geometry difference among these samples can be ascribed to the various TPA based on the reaction-induced crystallization mechanism [33]. At low dosage of TPA, the resultants were polyazomethine materials. With the increased TPA, the sheets were appeared on the sphere surfaces resulted from the crystallizing of more polyazomethine.

The structures of PLD/TPA polymers were investigate by Fourier transform infrared spectra (Fig. S1a in Supporting information). The absorption peaks at 1605 and 1690 cm^{-1} originate from C = N (the backbone structure for Schiff-bases) and C = O (the primary TPA) stretching vibration [34]. There are two broad but well-defined diffraction peaks at 26° and 44° in X-ray diffraction patterns (Fig. S1b in Supporting information), corresponding to the (002) and (001) reflections of amorphous carbon, respectively [35,36]. Raman spectra (Fig. S2 in Supporting information) of NOPCs exhibits two main broad bands at 1345 (D band, disordered phase) and 1590 cm^{-1} (G band, graphitic phase) [37]. The ratio of intensities of D-band to G-band (I_D/I_G) for NOPCs range from 0.82–0.93. The nitrogen adsorption–desorption isotherms of NOPCs shown in Fig. 2a exhibits type I sorption characteristics with a sharply increased adsorption capacity at $P/P_0 < 0.01$, indicating a microporous structure [38,39]. The pore size distributions (Fig. 2b) show regular and dominant ultramicropore size of 0.5–0.8 nm, matching the ion sizes of LiTFSI electrolyte ions (Li^+/TFSI– 0.069/0.79 nm [32]), which guides the orientation of Li^+/TFSI– ions along the pore extended direction and promotes the effective utilization of pore space in NOPCs, resulting in enhanced capacitance [20]. In addition, NOPCs also have large supermicropores of 1.2 nm which are beneficial for the fast transportation and diffusion of electrolyte ions [15]. The unique pore structure can be attributed to the internal skeleton cavity of the Schiff-base polymer, and the release of small molecular volatile matter resulting from the polymer decomposition during carbonization/KOH activation. NOPCs show high specific surface areas in the range of 928–1616 m^2/g, as shown in Table 1.

X-ray photoelectron spectroscopy (XPS) survey spectra of NOPCs demonstrate the presence of C, O, and N (Fig. S3a in Supporting information). In the high-resolution N 1s spectra, all samples display four deconvoluted peaks at 398.2, 399.5, 400.3 and 401.6 eV, corresponding to N-6 (pyridinic), N-5 (pyrrolic or pyridonic), N-Q (quaternary) and N-X (oxidized pyridinic nitrogen), respectively (Figs. S3b–e in Supporting information) [40,41]. N-6 and N-5 can induce *pseudo*-capacitance through faradic redox reaction, while N-Q and N-X promote the electronic transfer and the conductivity [42,43]. The O 1s region spectra can be deconvoluted into four peaks as follows: O-1 (C = O quinone type oxygen, 530.7 eV), O-2 (C–OH phenol group and/or C–O–C ether group, 532.1 eV), and *O*-3 (COO– carboxyl group, 533.6 eV) (Figs. S3f–i in Supporting information) [44]. The introducing of oxygen atoms also generate extra pseudocapacitance [15], attributed to high electronic transportation and excellent redox reversible ability of NOPCs. High bond energy of C = N and C = O (615/799 kJ/mol [45]) covalent bonds guarantee the maintenance of N (2.72%–3.41%) and O (9.77%–10.49%) species after carbonization (Table 1). The N/O atoms can play a synergetic effect in promoting the capacitive performance of NOPCs. Besides, wettability can improve the availability of electrolyte to the porous surface and greater utilization of the surface area to increase the capacitance [46,47]. The water contact angles on NOPC surfaces in Fig. 3. NOPCs wet a pure water droplet with the contact angles ranging from 50° to 62°, much lower than that of activated carbon (AC, 125°), suggesting a good hydrophilic ability.

Cyclic voltammetry (CV) and galvanostatic charge/discharge (GCD) measurements were first carried out using a three electrode system in 7 mol/kg LiTFSI solution. In Fig. S4a (Supporting information), CV profiles of NOPC electrodes at 10 mV/s in a voltage window of –1.1 V to 1.1 V display a slightly distorted rectangular-shape with a wide reversible hump, implying ideal electric capacity performance and the existence of pseudocapacitance characteristics due to the redox response of heteroatoms. GCD curves display nonlinear characteristics, also revealing the pseudocapacitive feature (Fig. S4b in Supporting information). Among these samples, $NOPC_1$ electrode has the largest specific capacitance of 204 F/g at 1 A/g due to the highest surface area and similar heteroatom content [48]. Besides, $NOPC_1$ shows the

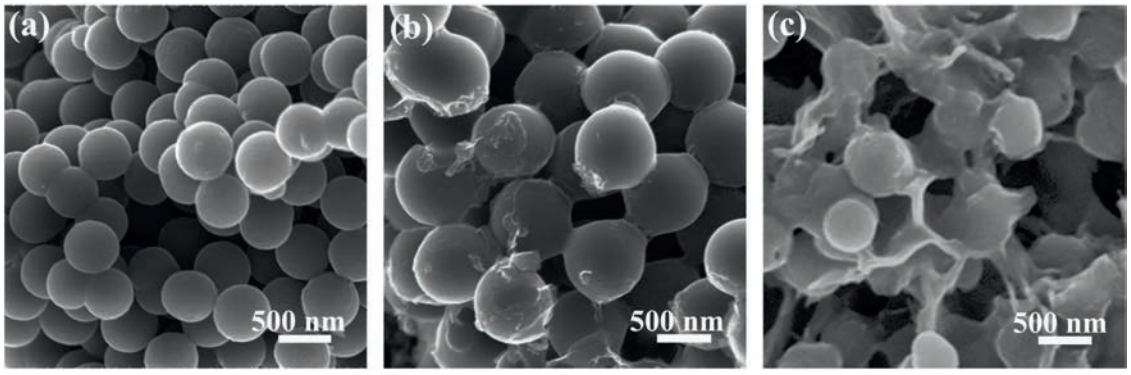

Fig. 1. SEM images of NOPCs: (a) $NOPC_{0.5}$, (b) $NOPC_1$, and (c) $NOPC_2$.

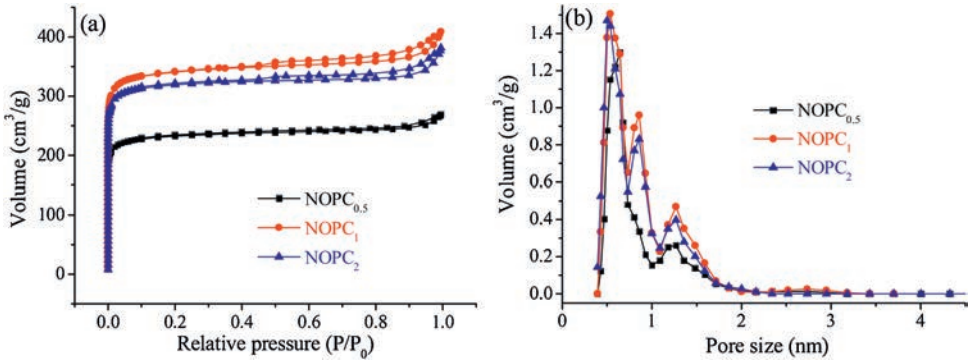

Fig. 2. Nitrogen sorption isotherms (a), and pore size distribution curves (b) of NOPCs.

Table 1
Specific surface area (S_{BET}), element composition and the contact angles of NOPCs.

Samples	S_{BET} (m^2/g)	Element content %			% of total N 1s				% of total O 1s			The contact angles (°)
		C	N	O	N-6	N-5	N-Q	N-X	O-1	O-2	O-3	
$NOPC_{0.5}$	931	86.97	3.26	9.77	25.3	24.0	30.7	19.0	22.3	47.7	30.0	53
$NOPC_1$	1366	86.73	3.41	9.86	29.0	25.8	31.4	13.8	16.2	48.7	35.1	50
$NOPC_2$	1284	86.33	3.27	10.41	22.9	16.0	45.6	15.5	3.8	56.2	40.0	55

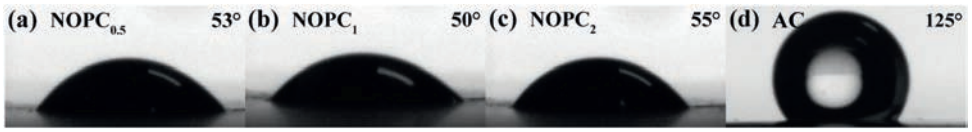

Fig. 3. The water contact angles on NOPCs surfaces.

smallest R_s (sum of the internal resistance of the electrode, ionic resistance of the electrolyte and contact resistance between electrode/current collector, obtained from the intercept of Nyquist plots) and lowest R_{ct} (interfacial charge transfer resistance, obtained from the diameter of the semicircles), as shown in Fig. S4c (Supporting information), which also contribute an enhanced electrochemical performance of $NOPC_1$ electrode. In addition, the electrode exhibits remarkable cycling stability (96.5% capacitance retention after 5000 cycles at 1 A/g), and almost 100% Coulombic efficiency (Fig. S4d in Supporting information).

Two identical NOPCs electrodes were assembled into a symmetric supercapacitor using a 2016 coin-type cell and 7 mol/kg LiTFSI aqueous solution as the electrolyte. Fig. 4a shows CV curves of the device at 10 mV/s in a potential window of 0–2 V. These profiles manifest quasi-rectangular shapes, with the highest integrated area in the profile of $NOPC_1$-loaded supercapacitor and

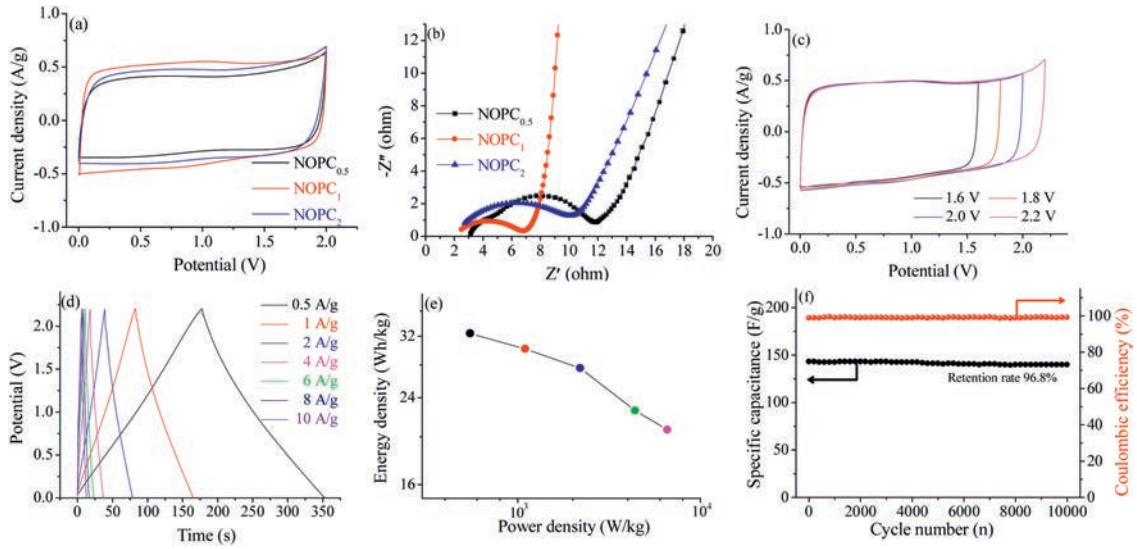

Fig. 4. (a) CV curves at 10 mV/s and (b) Nyquist plots of NOPCs-based devices using LiTFSI electrolyte; (c) CV curves of different potential windows at 10 mV/s; (d) GCD curves at various current densities; (e) Ragone plots, and (f) cycling performance of $NOPC_1$-loaded supercapacitor at 1 A/g.

consequently a largest capacitance. From the Nyquist plots shown in Fig. 4b, $NOPC_1$//$NOPC_1$ device exhibits the smallest R_s and lowest R_{ct}, indicating efficient ion and charge transportation [49]. In addition, a nearly vertical line in the Nyquist plots of $NOPC_1$-based device characterizes well capacitive behavior at low frequency [50]. At 10 mV/s, the maximum working voltage of $NOPC_1$//$NOPC_1$ configuration can reach to 2.2 V without obvious oxygen/hydrogen evolution peaks observed (Fig. 4c), manifesting a high oxidative stability of water molecules in LiTFSI electrolyte. The CV profiles at various scan rates ranging from 5 mV/s to 100 mV/s remain quasi-rectangular shapes, suggesting good reversibility of the charge-discharge process (Fig. S5a in Supporting information) [51]. Fig. 4d gives GCD curves of $NOPC_1$-based device at various current densities. The almost symmetric triangles imply that the device possesses a high Coulombic efficiency (98.1%–98.7%). To further characterize the durability of $NOPC_1$//$NOPC_1$ device, cycling was examined at progressively increased current densities and then returned to 1 A/g (Fig. S5b in Supporting information). After 700 cycles at varied current densities, the electrode capacitance still maintains to 151 F/g at 1 A/g, equating to ~98% of the initial value. Moreover, the capacitance retains its value for another 100 cycles without obvious decrease, manifesting outstanding durability at different current densities. In addition, after 10,000 cycles at 1 A/g, the capacitance retention rate and Coulombic efficiency of $NOPC_1$ electrode was still 96.8% and 98.1% (Fig. 4f), demonstrating an excellent long-term cyclic performance. The energy/power densities were calculated from the GCD charge/discharge curves based on $NOPC_1$//$NOPC_1$ configuration, as shown in Fig. 4e. Remarkably, the energy density of $NOPC_1$-based device reaches 30.4 Wh/kg at 1 kW/kg, higher than those of other carbon-based devices (Table S1 in Supporting information). In addition, the effect of different carbonization temperatures on pore structure, heteroatom contents and electrochemical performances was studied. CV and GCD curves (Figs. S6a and b in Supporting information) indicate that $NOPC_1$ obtained at 700 °C carbonization/activation exhibits the largest specific capacitance. When the temperature increases from 600 °C to 700 °C, the surface area increases from 959 m^2/g to 1366 m^2/g due to the adequate carbonization/activation. A higher carbonization temperature of 800 °C, although ensuring a decreased R_s (Fig. S6c in Supporting information), causes significant skeleton shrinkage, and thus results in the decreased surface area to 1087 m^2 g. While the nitrogen/oxygen contents decrease respectively from 3.62 at% and 3.41 at% to 2.29 at%, and from 11.04 at% and 9.76 at% to 7.31 at%, with increasing carbonization/activation temperature from 600 °C to 800 °C. Correspondingly, the specific capacitance of $NOPC_1$ electrode increases from 87 F/g to 151 F/g, and then decreases to 103 F/g at 1.0 A/g. A carbonization/activation temperature of 700 °C achieves an optimized balance between surface area and heteroatom content, and thus behaves a high electrochemical capacitance of the electrode.

In summary, we demonstrate a simple route to synthesize NOPCs based on *p*-toluenesulfonic acid-assisted amine-aldehyde Schiff-base reaction. The interconnected carbon spheres in a representative $NOPC_1$ provide a conductive network to benefit the charge transfer. Large surface area (1366 m^2/g) and electrolyte ion-matched micropores (0.5–0.8 nm) guarantee the generation of double-layer capacitance, and shorten the ion diffusion distance to the interior pore surfaces. Electrochemical active and hydrophilic N/O heteroatoms also contribute to the enhanced capacitive performance. Consequently, the resultant $NOPC_1$-based device using a 2.2 V LiTFSI WIS electrolyte gives a high energy output up to 30.5 Wh/kg at 1 kW/kg with high cyclic stability after successive 10,000 cycles (~96.8% capacitance retention at 1 A/g). The excellent electrochemical properties make NOPCs a promising electrode for efficient energy storage.

Acknowledgments

This work was financially supported by the National Natural Science Foundation of China (Nos. 21875165, 51772216 and 21703161), the Science and Technology Commission of Shanghai Municipality, China (No. 14DZ2261100), and the Fundamental Research Funds for the Central Universities.

Appendix A. Supplementary data

Supplementary material related to this article can be found, in the online version, at doi:https://doi.org/10.1016/j.cclet.2019.05.035.

References

[1] D. Jia, X. Yu, H. Tan, et al., J. Mater. Chem. A 5 (2017) 1516–1525.
[2] L. Miao, X. Qian, D. Zhu, et al., Chin. Chem. Lett. 30 (2019) 1445–1449.
[3] H. Yu, H. Xia, J. Zhang, et al., Chin. Chem. Lett. 29 (2018) 834–836.
[4] J. Zhao, Y. Li, F. Huang, et al., J. Electroanal. Chem. 823 (2018) 474–481.
[5] X. He, X. Li, H. Ma, et al., J. Power Sources 340 (2017) 183–191.
[6] X. He, H. Zhang, H. Zhang, et al., J. Mater. Chem. A 2 (2014) 19633–19640.
[7] Z. Liu, Z. Zhou, W. Xiong, et al., Langmuir 34 (2018) 10389–10396.
[8] J. Zhao, Y. Li, X. Chen, et al., Electrochim. Acta 292 (2018) 458–467.
[9] Y. Liu, N. Liu, L. Yu, et al., Chem. Eng. J. 362 (2019) 600–608.
[10] Y. Zhu, N. Li, T. Lv, et al., J. Mater. Chem. A 6 (2018) 941–947.
[11] H. Peng, G. Qian, N. Li, et al., Adv. Sci. 5 (2018) 1800784.
[12] J. Liu, N.P. Wickramaratne, S.Z. Qiao, et al., Nat. Mater. 14 (2015) 763.
[13] J. Pang, W. Zhang, H. Zhang, et al., Carbon 132 (2018) 280–293.
[14] S. Huo, M. Liu, L. Wu, et al., J. Power Sources 387 (2018) 81–90.
[15] D. Xue, D. Zhu, W. Xiong, et al., ACS Sustainable Chem. Eng. 7 (2019) 7024–7034.
[16] G. Zhu, L. Ma, H. Lv, et al., Nanoscale 9 (2017) 1237–1243.
[17] D. Reber, R.-S. Kühnel, C. Battaglia, Sustain. Energ. Fuels 1 (2017) 2155–2161.
[18] A. Gambou-Bosca, D. Bélanger, J. Power Sources 326 (2016) 595–603.
[19] G. Sun, W. Song, X. Liu, et al., Electrochim. Acta 56 (2011) 9248–9256.
[20] L. Zhang, Y. Guo, K. Shen, et al., J. Mater. Chem. A 7 (2019) 9163–9172.
[21] S. Dong, X. He, H. Zhang, et al., J. Mater. Chem. A 6 (2018) 15954–15960.
[22] X. Xie, X. He, H. Zhang, et al., Chem. Eng. J. 350 (2018) 49–56.
[23] C. Wang, D. Wu, H. Wang, et al., J. Mater. Chem. A 6 (2018) 1244–1254.
[24] H. Luo, P. Xiong, J. Xie, et al., Adv. Funct. Mater. 28 (2018) 1803075.
[25] Q. Wang, B. Qin, X. Zhang, et al., J. Mater. Chem. A 6 (2018) 19653–19663.
[26] C. Ramasamy, J. Palma del Val, M. Anderson, J. Power Sources 248 (2014) 370–377.
[27] K. Fic, G. Lota, M. Meller, et al., Energy Environ. Sci. 5 (2012) 5842–5850.
[28] Q. Dou, S. Lei, D.-W. Wang, et al., Energy Environ. Sci. 11 (2018) 3212–3219.
[29] L. Smith, B. Dunn, Science 350 (2015) 918.
[30] L. Suo, O. Borodin, T. Gao, et al., Science 350 (2015) 938–943.
[31] L. Suo, O. Borodin, W. Sun, et al., Angew. Chem. Int. Ed. 55 (2016) 7136–7141.
[32] P. Simon, Y. Gogotsi, Nat. Mater. 7 (2008) 845–854.
[33] L. Qiu, Y. Jiang, X. Sun, et al., J. Mater. Chem. A 2 (2014) 15132–15138.
[34] R. Zhang, X. Jing, Y. Chu, et al., J. Mater. Chem. A 6 (2018) 17730–17739.
[35] L. Yao, Q. Wu, P. Zhang, et al., Adv. Mater. 30 (2018) 1706054.
[36] T. Guan, K. Li, J. Zhao, et al., J. Mater. Chem. A 5 (2017) 15869–15878.
[37] L. Miao, D. Zhu, M. Liu, et al., Electrochim. Acta 274 (2018) 378–388.
[38] M. Liu, J. Niu, Z. Zhang, et al., Nano Energy 51 (2018) 366–372.
[39] M. Liu, F. Zhao, D. Zhu, et al., Mater. Chem. Phys. 211 (2018) 234–241.
[40] N. Zhang, F. Liu, S.-D. Xu, et al., J. Mater. Chem. A 5 (2017) 22631–22640.
[41] S. Witomska, Z. Liu, W. Czepa, et al., J. Am. Chem. Soc. 141 (2018) 482–487.
[42] J. Zhao, Y. Li, G. Wang, et al., J. Mater. Chem. A 5 (2017) 23085–23093.
[43] J. Zhao, J. Gong, Y. Li, et al., Acta Chim. Sinica 76 (2018) 107–112.
[44] Z. Song, H. Duan, L. Li, et al., Chem. Eng. J. 372 (2019) 1216–1225.
[45] D. Zhu, J. Jiang, D. Sun, et al., J. Mater. Chem. A 6 (2018) 12334–12343.
[46] D. Qu, J. Power Sources 109 (2002) 403–411.
[47] K.M. Horax, S. Bao, M. Wang, et al., Chin. Chem. Lett. 28 (2017) 2290–2294.
[48] F. Wei, X. He, H. Zhang, et al., J. Power Sources 428 (2019) 8–12.
[49] J. Jiang, P. Nie, S. Fang, et al., Chin. Chem. Lett. 29 (2018) 624–628.
[50] X. He, X. Xie, J. Wang, et al., Nanoscale 11 (2019) 6610–6619.
[51] H. Li, T. Lv, H. Sun, et al., Nat. Commun. 10 (2019) 536.